Full length article

Testing and modelling of butt-welded connections in thin-walled aluminium structures

Nguyen-Hieu Hoang [a,b,*], David Morin [b,c], Magnus Langseth [b,c]

[a] *Department of Materials and Nanotechnology, SINTEF Industry, Norway*
[b] *Centre for Research-based Innovation CASA, Norway*
[c] *Department of Structural Engineering, Norwegian University of Science and Technology, N–7491 Trondheim, Norway*

ARTICLE INFO

ABSTRACT

The present paper experimentally investigated the mechanical behaviour of butt-welded joints and evaluated suitable numerical approaches for modelling them in thin-walled structures with large shell-based models. Welded connections of both similar and dissimilar materials were first experimentally investigated. Two extruded plates in 6060 and 7003 in temper T6 were used as parent materials for Metal Inert Gas (MIG) welding. Three welded joints were made by combining the two parent materials. Extensive testing was carried out to investigate microstructure, hardness and mechanical stress–strain behaviour of the base materials, heat-affected zones (HAZ) and weld metals. Cross-weld tensile tests with two weld orientations (with respect to the loading direction) were performed to study the load–displacement and fracture behaviour of the welded joints. The experimental results were also used to provide inputs to calibrate and validate shell element-based models simulating the response of welded aluminium structures. Two modelling approaches were investigated. The first approach, which is a conventional "mechanical analysis", used material model inputs from the experimental testing, assuming uniform HAZ strength. The second modelling approach, which is proposed in this study for engineering applications, relies on inverse modelling of the load–displacement behaviour of similar material cross-weld tension tests to optimize the HAZ and weld properties. The newly proposed modelling approach was further verified based on a set of verification tests of cross-weld tension, using shell-based models with different mesh sizes. A good agreement between numerical and experimental results both in terms of load–displacement and fracture behaviour was obtained, suggesting that the novel modelling approach could be a reliable and efficient method for designing butt-welded aluminium structures.

1. Introduction

Aluminium alloys are today used extensively as structural materials in a wide variety of industries from oil and gas, physical security, automotive, aerospace, and energy due to its light weight, high strength, and high energy absorption capacity. For light-weight structure design in which dissimilar materials are involved, it is nearly impossible to have connection-free structures. Welding methods are conventionally used to join aluminium, and metals in generals, due to their low costs, speed, geometrical flexibility and desirable mechanical properties.

However, design of aluminium welded structural components is a rather challenging and time-consuming task. This is especially true when the manufacturing of welded components from aluminium alloys involves a series of thermal and mechanical operations. With age-hardenable aluminium alloys, the thermo-mechanical process due to welding results in the formation of narrow Heat-Affected Zones (HAZ) with a large variation of material properties. These potential weak zones may localize deformations when these components are subjected

to mechanical loads and cause significant problems with respect to structural integrity.

Even if design codes Eurocode 9 [1] give provisions for the design of welded aluminium connections, a robust, efficient and reliable modelling method to predict the load–displacement and fracture behaviour of these components in welded structure is still required.

Currently there is no unified approach to the problem of material failure in thin-walled aluminium structures, which considers the mechanical properties of the welds and HAZ, as well as the stress concentrations caused by the inhomogeneity of material properties in HAZ. However, modelling approaches of welded structures may generally be classified into two classes. The first approach, namely "thermal-microstructure-mechanical analysis", calls for the use of a rather sophisticated through-process simulation technique to reduce the need for extensive experimental testing for material model calibration and to enable realistic prediction of the mechanical performance of welded components and structures. In this approach, microstructure

---

and mechanical properties evolution within HAZ are calculated, accounting for large temperature gradients due to the welding process. A corresponding variation in the resulting microstructure and yield strength after welding can be simulated using microstructure based constitutive model, developed by e.g. Myhr et al. [2,3,4] for Al–Mg–Si alloys. The result from microstructure-based models is then further integrated into structural analyses to predict the load–displacement and failure response of welded structures as demonstrated by, e.g. Zhang et al. [5], Pickett et al. [6], Puydt et al. [7] and Nazemi [8]. In these authors' works, solid element based models were used, and the resulting numerical results were rather encouraging. However, this approach relies both on the capability of microstructure-based models to predict the properties of HAZ and a fine mesh resolution to be able to represent the gradient of material properties in HAZ. This may pose impracticality in industrial uses, especially for large structure modelling. Recently, Dørum et al. [9] have used a similar approach as Zhang et al. [5] to through-process simulate the structure and plastic failure behaviour of welded aluminium samples, using both solid and shell element-based models. Their work has shown that very small elements (much less than the plate thickness), together with non-local approach, are needed to resolve the large strain gradients within the HAZ in order to capture localization and predict failure properly. The proposed approach was further verified by Alisibramulisi [10] through an extensive testing programme of welded joints of Al–Mg–Si and Al–Zn–Mg alloys, covering various heat-treatment routes. The work has confirmed the need of having a reliable microstructure-based model for predicting the mechanical properties of HAZ undergoing different heat-treatment routes in the present approach.

The second modelling approach, namely "mechanical analysis", requires experimental testing to characterize the material properties of HAZ and to provide inputs for structural analyses of welded structure. This approach either assumes uniform HAZ strength for simplicity reason in design models [11,12] or considers the gradient of HAZ strength by discretizing the HAZ into multi-parts with different material properties as proposed, for instance by Wang et al. [13,14]. In these authors' work, the properties of the HAZ and weld were established based on tensile test data from the literature [15]. The strain localization and fracture in various welded aluminium connections were studied in their works using shell elements combined with an elastic–plastic constitutive model accounting for the anisotropy and damage of the aluminium alloy. Satisfactory agreement with experimental results was obtained. However, the proposed methodology requires extensive calibration test programme to provide inputs to the model. Tensile tests are conventionally used to characterize HAZ properties. However, more advanced characterization methods as proposed by Markiewicz and his co-authors [16,17] and may be needed when the size of joints and HAZ is not sufficient for direct specimen machining. In addition, modelling the HAZ with different small parts to account for the gradient of HAZ strength is time-consuming with respect to both the meshing and computation. This aspect may not be neglected when considering industrial large-scale structure analyses in which shell-based models with mesh size preferably greater than the plate thickness are used. Recently, Arif et al. [18] has proposed an efficient method in which multiple HAZ properties could be included in a single (large) shell finite element. This approach was successfully demonstrated for modelling laser welded joints in these authors' work. Alternatively, cohesive elements could be used to capture the plastic failure in the HAZ as investigated by Dørum et al. [9] and more recently by Woelke et al. [19].

In this paper, the main objectives are (1) to investigate the mechanical behaviour of welded aluminium alloys and (2) to propose and evaluate a modelling approach suitable for large shell element-based models of welded structures. To this end, welded connections of both similar and dissimilar materials were first experimentally investigated in Section 2. Two extruded aluminium alloys, 6060 and 7003 in temper T6, which are widely used in the automotive industry, were used as parent materials. Three welded joints were made by combining the two parent materials. Extensive testing was carried out to characterize microstructure, hardness and mechanical stress–strain behaviour of the base materials, HAZ and weld metals. Cross-weld tensile tests with two weld orientations (with respect to the loading direction) were performed to study the load–displacement and fracture behaviour of the welded joints. The experimental results were used to provide inputs for calibrating and validating shell element-based models established in Section 3. Two modelling approaches were investigated. The first approach, which is a conventional "mechanical analysis", used material model inputs from the experimental testing, assuming uniform HAZ strength. The predictive capability of the conventional "mechanical analysis" was first studied and discussed. The second approach, which is proposed in the present work, relies on inverse modelling of cross-weld tension behaviour of similar materials joints to optimize the HAZ and weld properties. The performance of the proposed approach was further verified using a set of verification tests of cross-weld tension, using shell element based models with different mesh sizes. Finally, concluding remarks are summarized and discussed in Section 4.

2. Experimental study

2.1. Materials and welding

The parent materials used in this study were two extruded aluminium alloys, namely 6060 and 7003 in T6 temper. Both alloys were heat-treatable, with 6060 being a typical Al–Mg–Si alloy, while 7003 belonging the Al–Zn–Mg based alloy family. The 3 mm-nominal thick extruded plates made of these aluminium alloys were welded together using Metal Inert Gas (MIG) welding, making three joining configurations in total, i.e. Joint C1 (6060–6060 welded joint), Joint C2 (7003–7003 welded joint) and dissimilar material Joint C3 (6060–7003 welded joint). The welding process was performed by Fronius Robot using the advanced Cold Metal Transfer (CMT) Pulse technique, i.e. a combination of CMT and pulsed arc, to increase the process window (i.e. the power range) during the welding. An 1.2 mm diameter wire in 5183 alloy was used as filler material with a feeding speed of 10.2 mm/min. The investigated aluminium plates were welded at 16 mm/second speed. All the welding process was done along the extrusion direction (ED) of the plates to be joined, see Fig. 1a for illustration. No post-weld heat-treatment (PWHT) was applied, and the welded samples were naturally aged in air prior to any further testing.

2.2. Materials investigation

2.2.1. Microstructure

Light optical microscope was used to investigate the grain structure of as-received alloys. Through-thickness samples along the extrusion direction (ED) of the extruded plates were mechanically grounded, polished and subsequent anodized prior to the examination in the microscope. Fig. 2 shows the grain structure of the two investigated alloys. As seen, the 6060 alloy has a typical recrystallized grain structure, while the 7003 alloy possessing a fibrous microstructure. Small cortical layers, which exhibit a recrystallized grain structure, are present close to the surface of the extruded 7003 alloy. This is a result from the high shear rate close to the surface in interaction with the extrusion die during the extrusion process.

2.2.2. Mechanical properties

The mechanical behaviour of the as-received alloys was investigated using tensile test specimens machined both in the extrusion and transverse directions. The samples geometries are shown in Fig. 1b and c. The flat dog-bone sample, Fig. 1b, was used to investigate material properties in the transverse direction. On the contrary, the smooth cylindrical specimen, Fig. 1c, was used for tests in the extrusion direction for the sake of comparison with HAZ properties as investigated
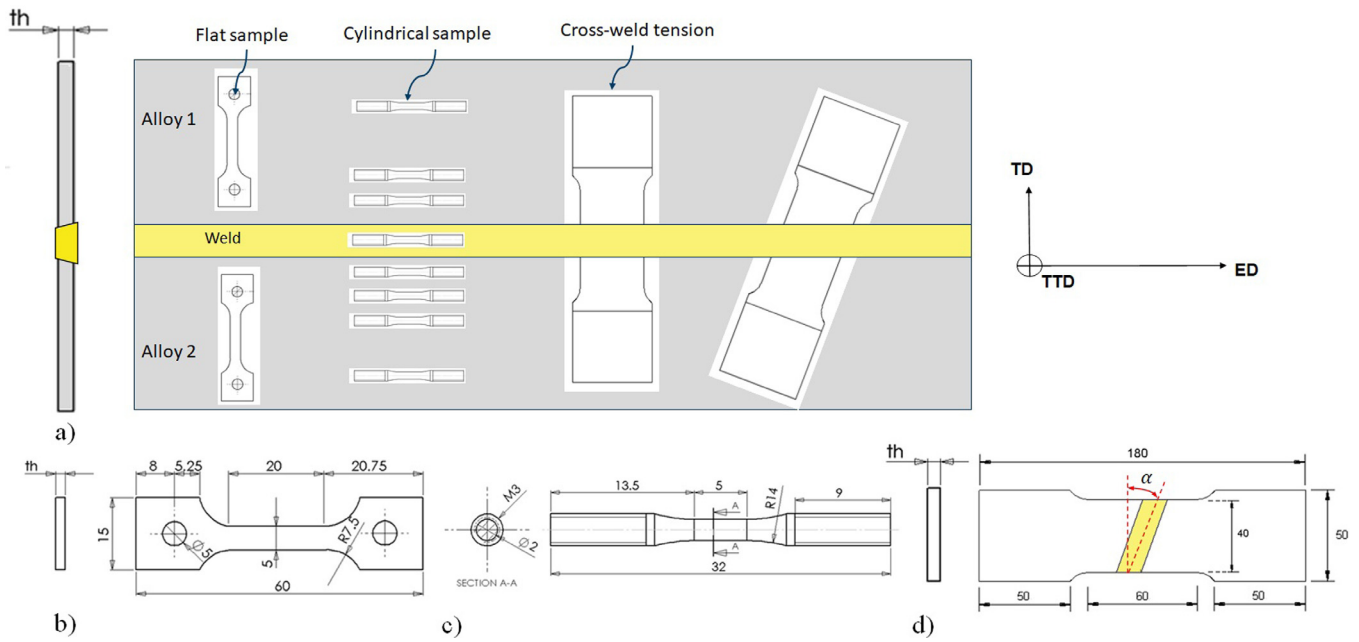
Fig. 1. (a) Illustration of dissimilar welded plates, (b) Flat tensile test specimen, (c) cylindrical tensile specimen and (d) cross-weld tension specimen. TTD, TD and ED respectively denote through-thickness, transverse and extrusion directions.
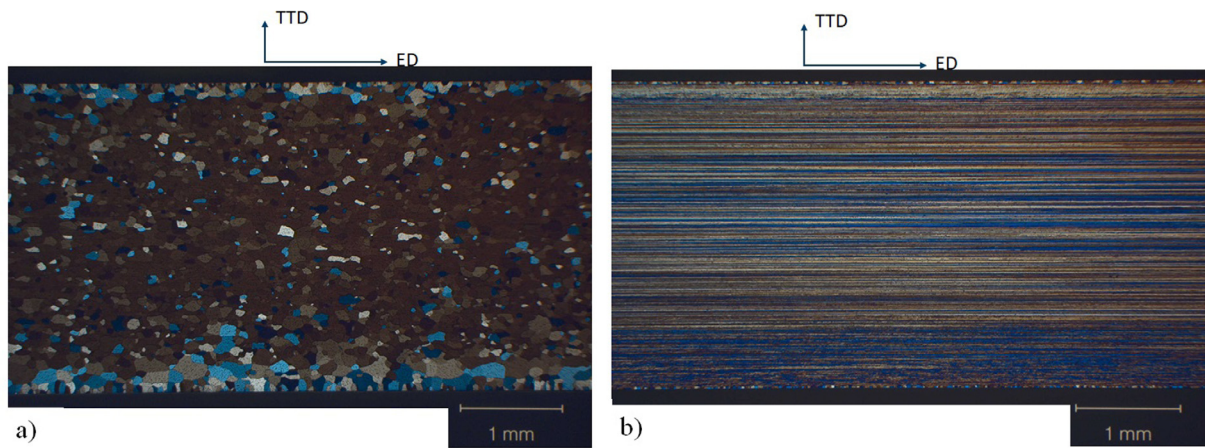

Fig. 2. Microstructure of: (a) 6060 alloy and (b) 7003 alloy. The microstructure was investigated in the transverse direction of extruded plates. TTD and ED denote respectively the through-thickness and extrusion directions.

further in Section 2.3.2 using the same sample geometry. All the tensile tests were performed under displacement control with a nominal quasi-static strain rate (i.e. 0.5E−3/s) using a Zwick Z030 universal testing machine with a 30 kN load cell. Three repetitions were carried out for each test. The test setups are shown in Fig. 3a and b, for the testing of the flat and cylindrical specimens respectively.

For the flat samples (in the transverse direction, see Fig. 1a), an extensometer of 15 mm gauge length was used to monitor the strain of the tested samples. Fig. 4 shows representative engineering stress–strain curves up to fracture for the two investigated alloys in the transverse direction (TD). The obtained test results are very repetitive. As can be seen, 7003 is a high-strength alloy with proof and tensile strengths twice as large as those of 6060 alloys. The investigated alloys are ductile, with a pronounced neck as illustrated in Fig. 4.

For the smooth cylindrical samples (along the extrusion direction ED, see Fig. 1a), diameter reductions in the transverse and through-thickness directions (denoted d_{TD} and d_{TTD}, respectively) were continuously measured at the minimum cross-section all the way to fracture by a laser-scan micrometer, see Fig. 3b [20]. Assuming plastic incompressibility, the true stress σ and logarithmic strain in longitudinal direction ε are calculated from the measured force F and the diameters d_{TD} and d_{TTD} as:

$$\sigma = \frac{F}{A}, \quad \varepsilon = ln\left(\frac{A_0}{A}\right) = ln\left(\frac{d_0^2}{d_{TD}d_{TTD}}\right) \tag{1}$$

where A_0 and A are respectively the initial cross-section area and the actual area of the specimen, while d_0 is its initial diameter.

The true stress versus longitudinal true strain curves are plotted in Fig. 5 for the two investigated alloys in both ED and TD. Using the flat specimens (Fig. 1b), the true stress–strain curves in TD are plotted up to necking, since the local deformation in the necked area could not be monitored with the used extensometer after the incipient necking. On the contrary, the possibility to monitor the diameter reduction in the necked area with the laser-scan micrometer enabled the interpretation of true stress–strain results in ED all the way to fracture, see Fig. 5. As seen, the two alloys exhibited to some extent anisotropy both in yield stress and work hardening, with a higher strength in ED. The 6060 alloy is more ductile in comparison with the investigated 7003 alloy, as seen from the strain at fracture in ED.
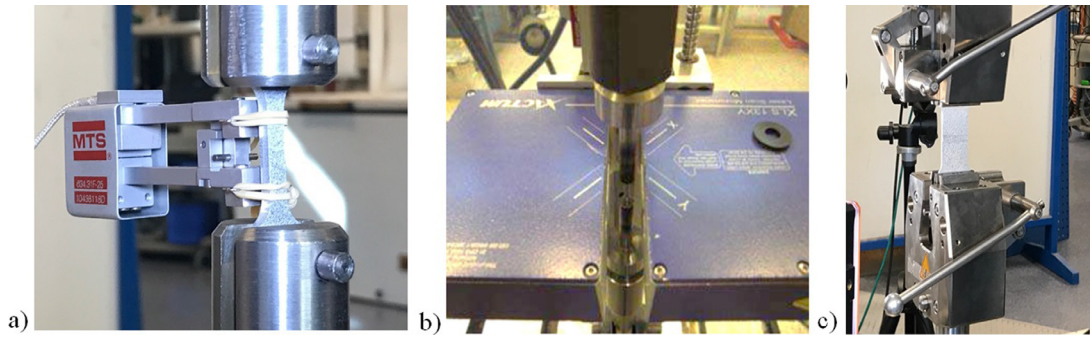
Fig. 3. Material test setups: (a) flat sample, (b) cylindrical sample and (c) Cross-weld tension test setup.
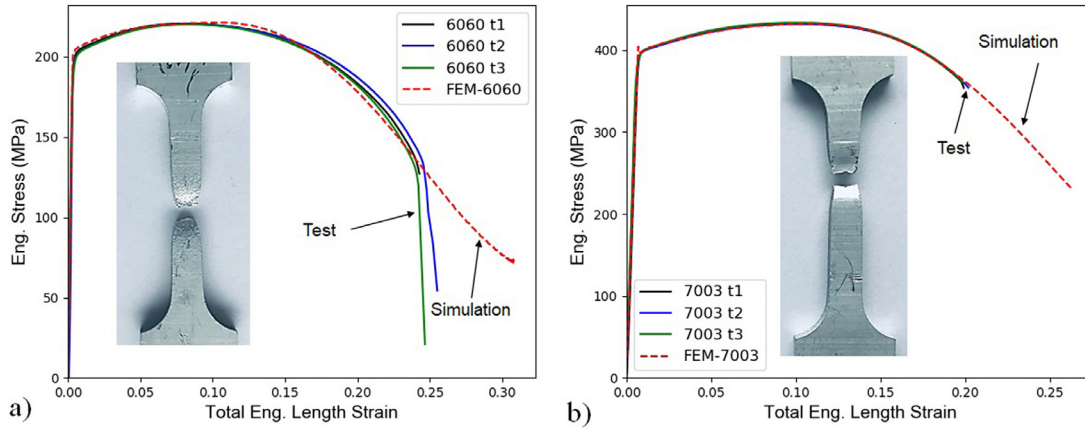

Fig. 4. Engineering stress–strain curves in transverse direction (TD) from flat sample tensile tests of 6060 and 7003 alloy. Three repetitive test results are plotted together with the numerical simulation result (dashed red curve).
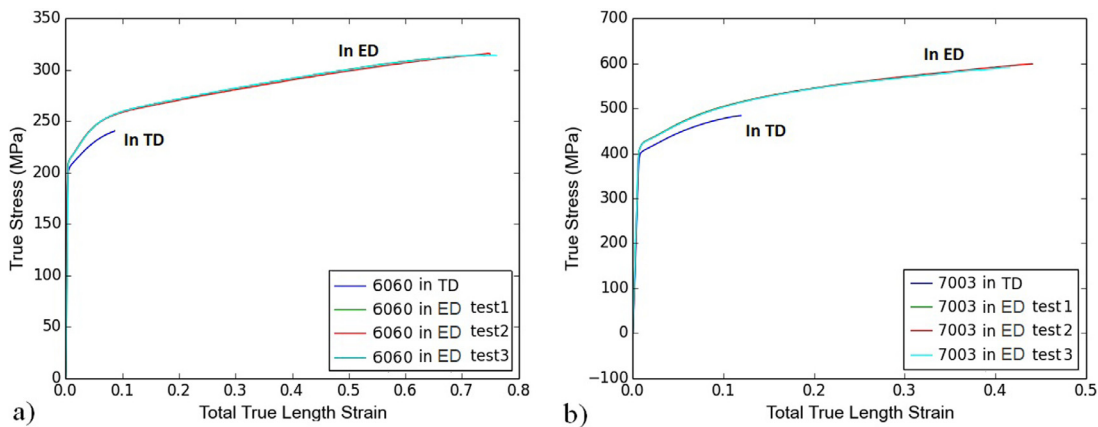

Fig. 5. True stress–strain curves in ED and TD, (a) 6060 alloy and (b) 7003 alloy.

2.3. Welded connections testing

2.3.1. Microstructure and hardness investigation

The microstructure and hardness of the three welded joints, namely Joint C1 (6060–6060 welded joint), Joint C2 (7003–7003 welded joint) and dissimilar material Joint C3 (6060–7003 welded joint), were investigated using the samples shown in Fig. 6a. The samples were mechanically ground, polished and subsequently anodized prior to the examination in the light optical microscope for grain structure investigations, as for the material study. The hardness measure was then performed along the welds (in TD) by micro indentation using LEICA VMHT MOT test machine and 1 kg load.

Fig. 6b shows the hardness result in Vickers hardness (HV) along the cross weld, i.e. as function of the distance from the weld centre. As expected for the two similar material joints C1 and C2, the measured hardness is symmetric with respect the weld centre. The HAZ widths of Joint C1 and Joint C2 are about 8.5 mm and 12.5 mm, respectively. The transition area (from HAZ to the base material) of the two joints are comparable and close to 4 mm. It can be seen that the softest zone of Joint C1 is the HAZ, while for Joint C2 it is located in the butt-weld area. The hardness values of HAZ of the two joints C1 and C2 are about 37% and 14% lower than that of the corresponding parent materials. The dissimilar material Joint C3 represented a good mix of the two joints C1 and C2, as indicated by the hardness results. It is of interest to see that the butt-weld's hardness of Joint C3 is about the average of those of Joint C1 and C2.

The optical microscope images of the three joints are shown in Fig. 7. The HAZ of Joint C1 has a recrystallized grain structure, with a
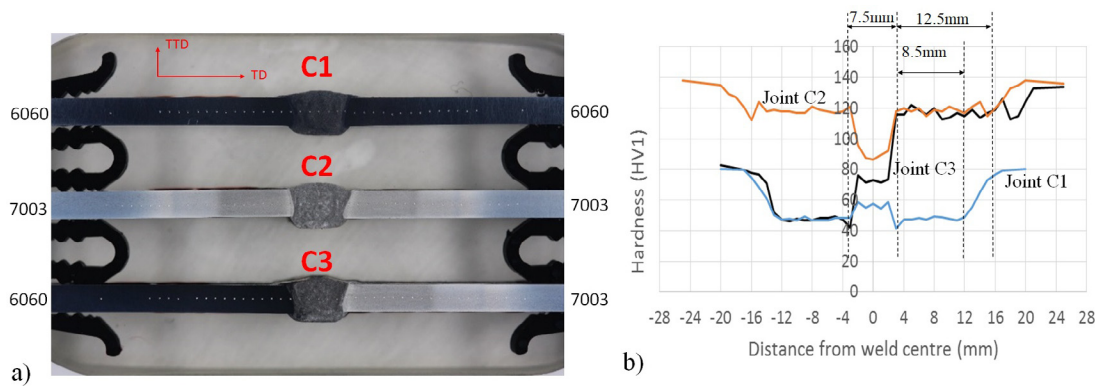
Fig. 6. (a) Samples for microstructure and hardness investigation, (b) Hardness test results of three joints. TTD and TD respectively denote the through-thickness and transverse directions.
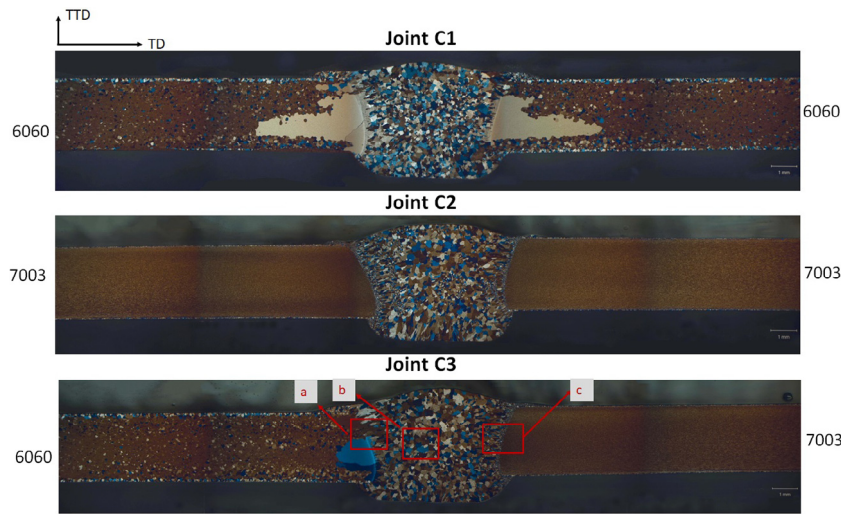

Fig. 7. Microstructures of the three investigated welded joints. TTD and TD respectively denote the through-thickness and transverse directions.

significant grain size variation. Some very large grains were observed close to the weld fusion area. The large grains were also observed on the welded 6060 side of Joint C3, but somewhat smaller. The reason for the resulted large grain in HAZ of the welded 6060 alloy is unknown and considered out of scope of the current study. Due to the fibre direction of the 7003 base material aligned in the extrusion direction (ED), see Fig. 2b, the fibrous grains of this alloy are seen as a cloud of "points" in Fig. 7 of the cross-weld sections perpendicular to ED. With this in mind, the HAZ of the welded 7003 alloy seems to also possess a fibrous grain structure as it can be seen from Fig. 7.

The butt-welds of the three joints have a recrystallized microstructure with coarser grains (about 200 μm) in comparison with the 6060 alloy grain size. It is interesting to see that on the side of the welded 7003 alloy, there is a grain size gradient towards the weld fusion line, which is not seen on the side of the welded 6060 alloy. Fig. 8 shows a zoom of the microstructure at different locations (namely a-Weld fusion with 6060 alloy, b-Weld material and c-Weld fusion with 7003 alloy) from Joint C3. As can be seen, the weld fusion on the side of the welded 7003 alloy serves as a transition area from the recrystallized grain structure of weld materials to fibrous grain structures of the HAZ.

2.3.2. Weld and HAZ material investigation

To get an insight into the mechanical properties of the HAZ and weld materials for the three joints, tensile tests were conducted using smooth cylindrical tensile specimens machined from the welded plates along the extrusion direction. Samples from two locations in HAZ of the welded 6060 alloy, three in HAZ of the welded 7003 alloy and one

sample in the centre of their weld materials were machined, see Fig. 9 for illustration. Three repetitions were performed for each test, leading to 24 mechanical tests. The geometry of the used smooth cylindrical tensile specimens was the same as for the base material testing, see in Fig. 1b. The same testing procedure for cylindrical tensile specimens as described in Section 2.2.2 was applied, using the setup with the laser-scan micrometer, see Fig. 3b.

Fig. 9 shows the true stress–longitudinal true strain results for all the tests, plotted all the way to fracture using Eq. (1). As for the base material testing, no significant scatter in results was observed in between the replicates. Thus, only one representative curve was shown in Fig. 9 for each test for sake of clarity. The comparison of the tensile behaviour between HAZ, weld metal and base materials is shown in Fig. 9a and b, respectively for the similar material welded joints C1 (6060–6060 joint) and C2 (7003–7003 joint). As can be seen, the yield stress of Joint C1's weld materials is slightly higher than that of the HAZ. The opposite is obtained for Joint C2. This observation is consistent with the hardness results shown in Fig. 6b. In Joint C1, the weld metal exhibits a stronger work-hardening behaviour in comparison with 6060 base material and HAZ materials, while the highest work-hardening was seen for HAZ materials in Joint C2. With respect to ductile fracture, the HAZ materials of Joint C1 exhibit a higher ductility than that of the weld material while the HAZ materials of Joint C2 exhibit a lower ductility than their corresponding weld material. A slight difference in tensile behaviour between the two HAZ tests of welded 6060 alloy (C1) is visible (Fig. 9), while the stress–strain curves from the three investigated locations in HAZ of Joint C2 are almost identical.
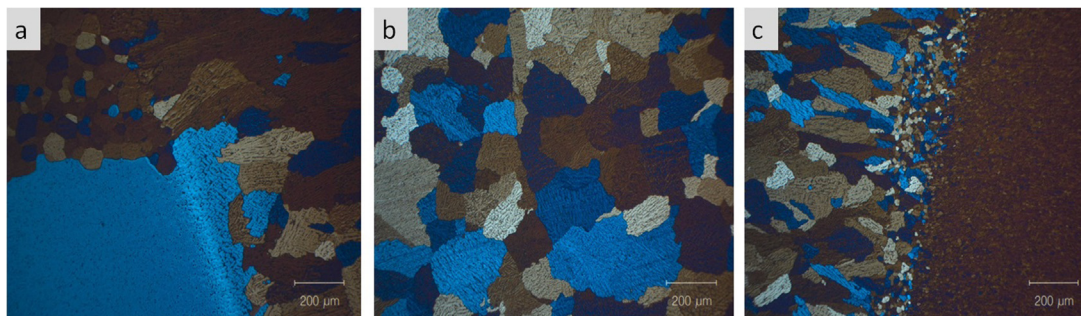
Fig. 8. Zoom of microstructure of Joint C3 (6060–7003 joint) at different zones illustrated in Fig. 7: (a) Weld fusion with 6060, (b) Weld material and (c) Weld fusion with 7003.

The true stress–longitudinal true strain results of the weld materials from the three joints are plotted together for comparison in Fig. 9c. As expected, the stress–strain curve of the weld material of Joint C3 (i.e. 6060–7003 joint) lies between those of the two other similar material joints, which is consistent with the hardness results in Fig. 6b. The ductility of Joint C3's weld material is in the same extent as for Joint C2, which is much lower than that of Joint C1 (6060–6060 joint). The stress–strain results also depict a serrated yielding at the first part of the curve (prior to necking) for all weld materials, see Fig. 9d showing a zoom of welds' stress–strain curves. The observed serration in yielding is related to the Portevin–Le Chateliers effect (PLC), occurring with dynamic strain ageing (DSA) associated with conditions when point defects can diffuse towards mobile dislocations and temporarily arrest them [21–23]. The DSA mechanism is widely observed for Al–Mg alloy family [22–26], including the 5182 alloy used as the weld filler material in this study. The observed serration in yielding is more pronounced for Joint C1, and less pronounced for Joint C2. This is most likely due to the mixing of the filler material and base material during the welding process, altering the Mg content as a function of the chemical composition of the welded base material.

Fig. 10 shows the representative test results for all the tested HAZ and weld materials, in terms of the engineering stress plotted against the engineering strains in both the trough-thickness and transverse directions (TTD and TD). The engineering strains e_{TTD} and e_{TD} are defined as:

$$e_{TTD} = \frac{d_0}{d_{TTD}}, \ e_{TD} = \frac{d_0}{d_{TD}} \tag{2}$$

where d_0, d_{TTD} and d_{TD} are respectively the initial diameter and the actual diameters in the through-thickness and transverse directions. Using these definitions, it can be observed that both alloys exhibit plastic anisotropy. The HAZ materials of the welded 7003 alloy are less ductile than those of the welded 6060 alloy, and fracture occurred prior to any observed necking with a typical shear fracture surface, see Fig. 10. On the contrary, the weld materials appear to be rather isotropic since no significant differences in strains in TTD and TD were observed for the three welded connections.

2.3.3. Cross-weld tensile tests

Cross-weld tensile samples were machined from the welded plates as illustrated in Fig. 1a to investigate the mechanical properties of the welded joints. The sample geometry is illustrated in Fig. 1d, with the butt-weld oriented in an angle α with respect to the transverse direction of the samples (i.e. the direction perpendicular to the loading direction).

The cross-weld tension behaviour of three welded joints was first tested in $\alpha = 0°$ (i.e. the weld direction perpendicular to the tensile loading direction). These tests were used for the numerical models calibration/verification in Section 3. Additional tests of Joint C1 (welded 6060–6060) and Joint C3 (welded 6060–7003) using samples in $\alpha = 20°$ with respect to the weld direction were also performed for a more reliable verification/validation of the modelling approaches investigated in

Section 3. Due to lack of materials, testing of Joint C2 (welded 7003–7003) in $\alpha = 20°$ was not possible. In the following, all the tests are labelled as $Cx - W\alpha$, with Cx denoting the joint configuration (i.e. C1, C2 and C3), and $W\alpha$ denoting the orientation of the butt-weld (i.e. W00 and W20).

The cross-weld tension testing was performed at quasi-static strain rate (i.e. 1e-3/s) under displacement control, using an Instron testing machine with a 250kN load cell, see Fig. 3c for the test setup. During testing, an extensometer of 40 mm gauge length was used to monitor the strain of the tested samples. At least three repetitions were carried out for each test.

Fig. 11 shows the cross-welds tensions behaviours for all successful tests in terms of engineering stress and engineering strain in the loading direction. For Joints $Cx - W00$ (i.e. weld angle $\alpha = 0$), the tests were performed with both full butt-weld and polished flat butt-weld, while for Joints $Cx - W20$ (i.e. weld angle $\alpha = 20$) only tests with flat butt-weld were investigated, see Fig. 11 for illustration.

As seen from the test results of Joints $Cx - W00$, the butt-weld geometry affected slightly the cross-tension behaviour (full lines for tests with full butt-welds, and dashed lines for tests with polished flat ones). Joint C1 of welded 6060–6060 alloys exhibits higher ductility in comparison with Joint C2 of welded 7003–7003 alloys. A localized thinning followed by softening was observed for Joint C1 tests, while Joint C2's samples failed prior to any necking with a typical through-thickness shear fracture mode. The fracture of C1 samples was located in the transition area (from HAZ to BM, about 8 mm from the weld fusion line), while the Joint C2's samples fractured in the weld area, see Fig. 11. The dissimilar material 6060–7003 joints (Joint C3) experienced similar mechanical and fracture behaviours as for Joint C1 (6060–6060), with a major deformation occurring on the 6060 side. Ductile fracture was also observed for the 6060–7003 joints at the transition area (from HAZ to BM, about 8 mm from the weld fusion line) on the 6060 side.

The joints with 20° oriented weld (i.e. Joints $Cx - W20$) exhibit similar behaviour in terms of engineering stress–strain curves as for Joints $Cx - W00$. Ductile fracture was obtained for all the investigated joints, $C1 - W20$ and $C3 - W20$, at the transition area (from HAZ to BM) on the 6060 side.

3. Numerical modelling of welded joints

This section aims to establish and investigate modelling approaches using large shell-element based models for simulating the load–displacement and fracture behaviour of welded connections in thin aluminium plate structures. Two modelling approaches were investigated. In the first approach, which is a conventional "mechanical analysis", the material model parameters for HAZ, weld and base materials were obtained from the calibration based on the experimental test results in Section 2. The second approach, which is novel, relied on inverse modelling of the cross-weld tension behaviour of similar materials joints to obtain the HAZ and weld material model parameters. Required inputs data for each approaches were calibrated, by using the
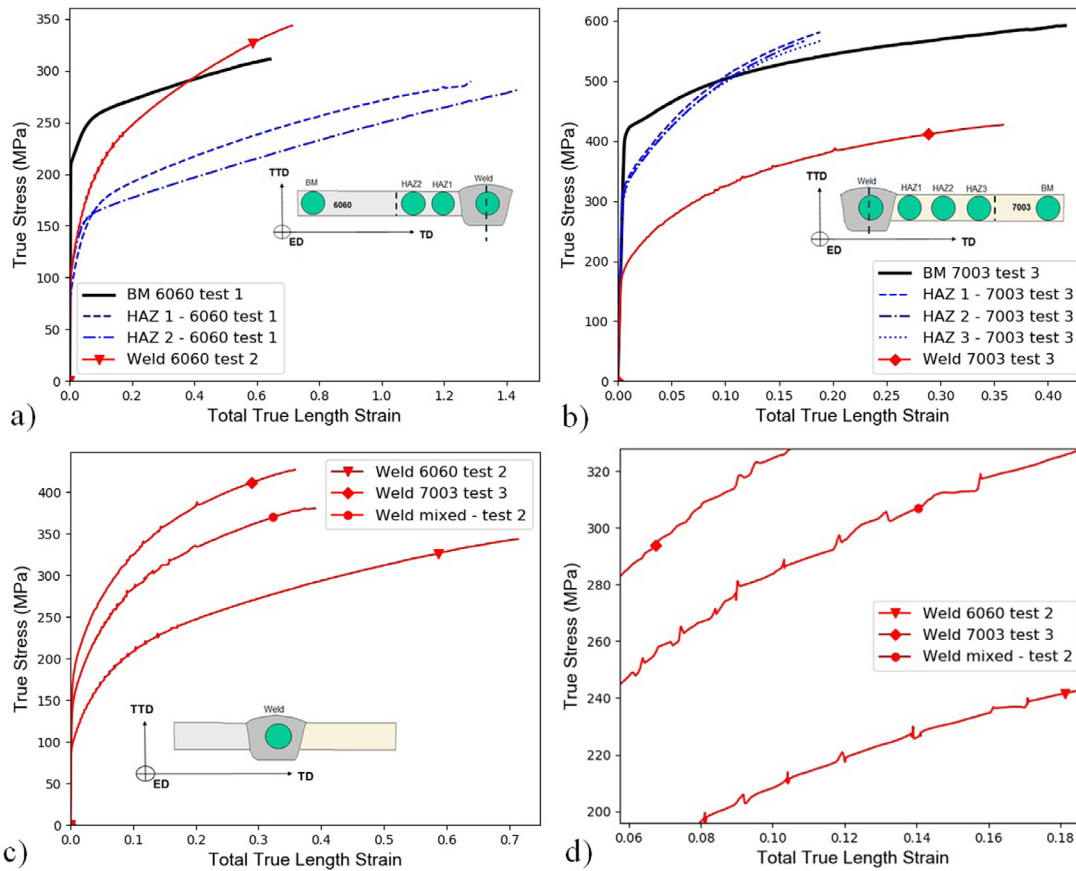
Fig. 9. Tensile behaviour of HAZ and weld materials of (a) Joint C1 (6060–6060 joint) and (b) Joint C2 (6060–7003 joint), (c) comparison of weld materials behaviour of the three joints, and (d) a zoom of weld materials' stress–strain curves.

available experimental results. The predictive performance of the two approaches were then investigated and discussed with respect to a set of verification tests of cross-weld tension.

3.1. Numerical models of cross-weld tension tests

Numerical models of all the cross-welds tension tests were established using the commercial non-linear explicit finite elements code, LS-DYNA, see Fig. 12a. A typical industrial mesh size of 4 mm was applied to all the models. The clamped parts of the test samples were modelled as rigid bodies, with the lower part constrained in all directional movements while a controlled upward displacement was applied to the top clamped part. All the other parts representing the geometries of the weld, HAZ and base material (BM) were modelled as deformable materials. It can be seen from Fig. 12a that two and three elements were used to discretize HAZ parts, respectively for the welded 6060 side and the welded 7003 side. The weld area was modelled as one part, with two elements of 4 mm mesh size. The present discretization was chosen in accordance to the width of HAZ of welded 6060 and 7003 sides and the weld areas, as shown in Fig. 6b. Due to the explicit nature of the finite element solver, a careful attention was paid to select an adequate loading velocity applied to the moving clamped part to avoid any dynamic related issues.

The material model used for the deformable materials is assumed to adopt an isotropic work-hardening law, the Hershey–Hosford yield criterion [27] for isotropic plasticity and associated flow rule. The yield function can be expressed as:

$$f = \sigma_{eq} - \sigma_y \tag{3}$$

where σ_{eq} is the equivalent stress and σ_y represents the flow stress.

The equivalent stress is defined in accordance to the Hershey–Hosford yield criterion for isotropic plasticity as:

$$\sigma_{eq} = \left[\frac{1}{2} \left(|\sigma_1 - \sigma_2|^m + |\sigma_2 - \sigma_3|^m + |\sigma_3 - \sigma_1|^m \right) \right]^{\frac{1}{m}} \tag{4}$$

where σ_1, σ_2, and σ_3 are the principal stresses of Cauchy stress tensor, while m is the parameter governing the shape of the yield function.

The flow stress is defined as follows:

$$\sigma_y = \sigma_0 + \sum_{i=1}^{2} Q_i \left[1 - exp\left(-\frac{\theta_i}{Q_i} \varepsilon_p \right) \right] \tag{5}$$

in which ε_p and σ_0 are respectively the equivalent plastic strain and the initial yield stress, while Q_i and θ_i are the extended Voce law's parameters defining the isotropic work-hardening behaviour.

Although the investigated materials exhibit plastic anisotropy as shown in Section 2, they were modelled as isotropic within this study. This simplification was recently shown to be acceptable in large scale analyses of aluminium extrusions under large deformations [28]. The exponent m of the Hershey–Hosford yield surface was set to $m = 8$ as usually assumed for FCC alloys [29,30].

The material model parameters for the base materials were taken from tests in the transverse direction (TD) using the flat specimens. The yield stress and working hardening parameters for 6060 and 7003 base materials were first calibrated using the true stress–true strain curves up to the diffuse necking point, see Fig. 5. However, in order to describe the work hardening behaviour of the material beyond the necking point to the final fracture with a reasonable accuracy, the Voce parameters were refined by inverse modelling of the tensile tests with flat samples in TD. A 3D solid element-based model was established in LS-DYNA, see Fig. 13a showing a half model of the flat sample tensile test owing to symmetry. A reasonably fine mesh size of 0.25 mm × 0.25 mm and
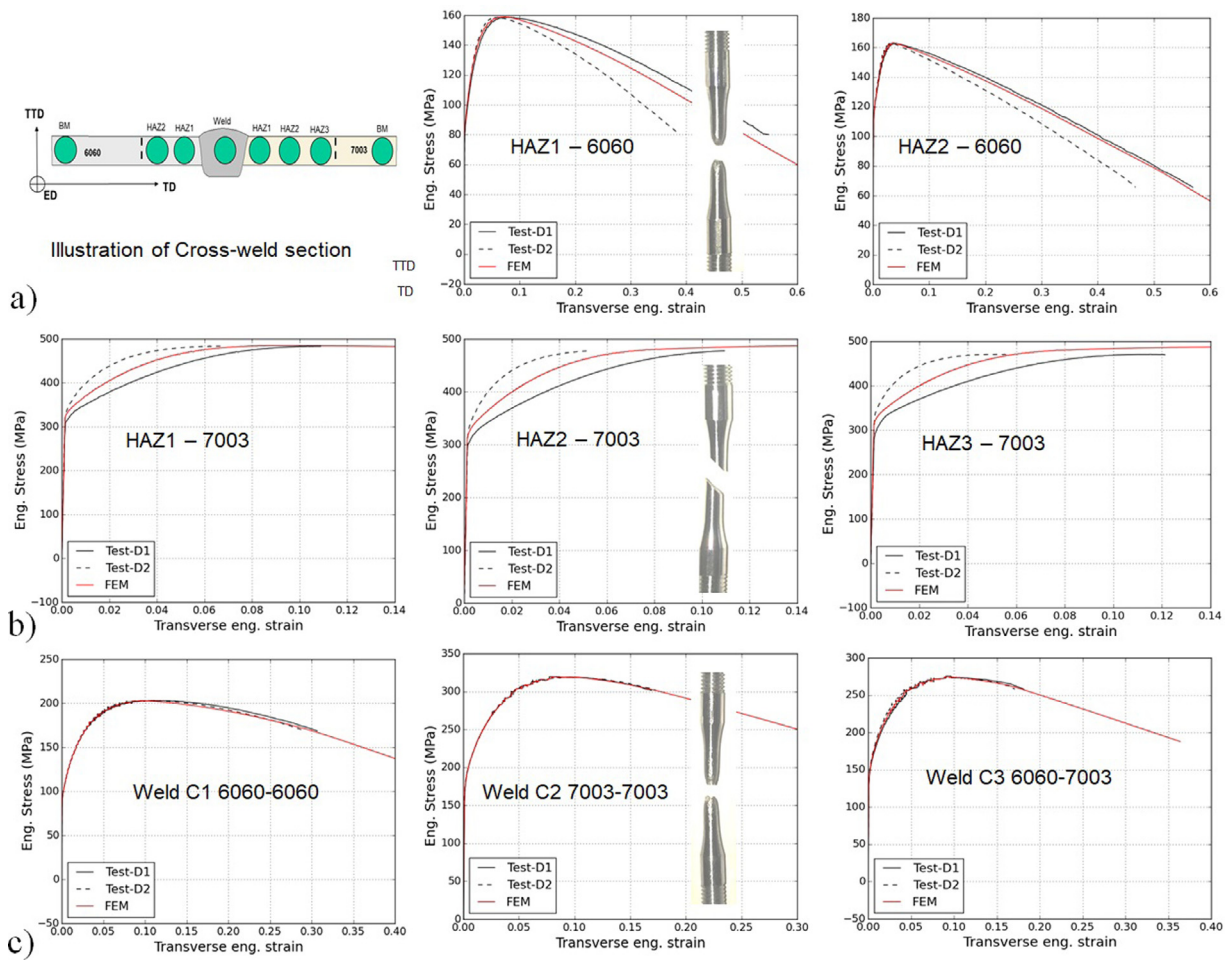
Fig. 10. Comparison between experimental and numerical results for HAZ and weld material tests: (a) HAZ materials of welded 6060 alloy, (b) HAZ materials of welded 7003 alloy and (c) weld materials of the three welded joints.

Table 1
Material parameters.

Materials	σ_0 in TD (MPa)	σ_0 in ED (MPa)	Q_1 (MPa)	θ_1 (MPa)	Q_2 (MPa)	θ_2 (MPa)	Notation
BM 6060	198	210	5.95	9043.2	65.6	722.0	[a]
BM 7003	399	410	27.7	580.44	109.7	874.3	[a]
HAZ 6060	89	94	78.1	2263.8	64.4	83.2	[a]
	85	85	439.8	642	116.5	498.5	[b]
HAZ 7003	304	313	139.0	3001.5	2758.5	765.5	[a]
	318	318	38.9	2162.2	4123.5	1168.6	[b]
Weld C1	90	90	38.5	3717	202.7	1722	[a]
	115	115	495.9	716.2	273.6	5088.7	[b]
Weld C2	156	156	40.5	7475.7	227.7	2157.0	[a]
	215	215	134.5	861.3	4405	603	[b]
Weld C3	131	131	99.4	2249.7	134.2	373.0	[a]
	165	165	632.6	885.2	153.7	2760.9	[b]

[a] Parameters calibrated using tensile tests.
[b] Yield stress derived from Eqs. (8), (9), and hardening parameters obtained by inverse modelling shown as an example for the 4 mm mesh models.

eight-node solid elements with one integration point were used for the numerical model. As seen in Fig. 4, the numerical results in terms of engineering stress–engineering strain were in a good agreement with the tests up to the final fracture for both 6060 and 7003 alloys.

Due to the geometrical restrictions imposed by the HAZ and butt-weld materials, the tensile test results were available only in the extrusion direction (ED). Thus, the material properties of the HAZ and welds were first calibrated using the test results this direction ED. With

the laser-scan micrometer, the true stress–strain data are available up to fracture for these tests, see Fig. 9.

Prior to necking, the true stress is identical to the equivalent stress for the uniaxial tensile testing. To estimate the equivalent stress–strain curves after the onset of necking, the Bridgman correction is used for the smooth samples, neglecting the anisotropy effect. The equivalent stress σ_{eq} is accordingly expressed as function of the true stress σ as
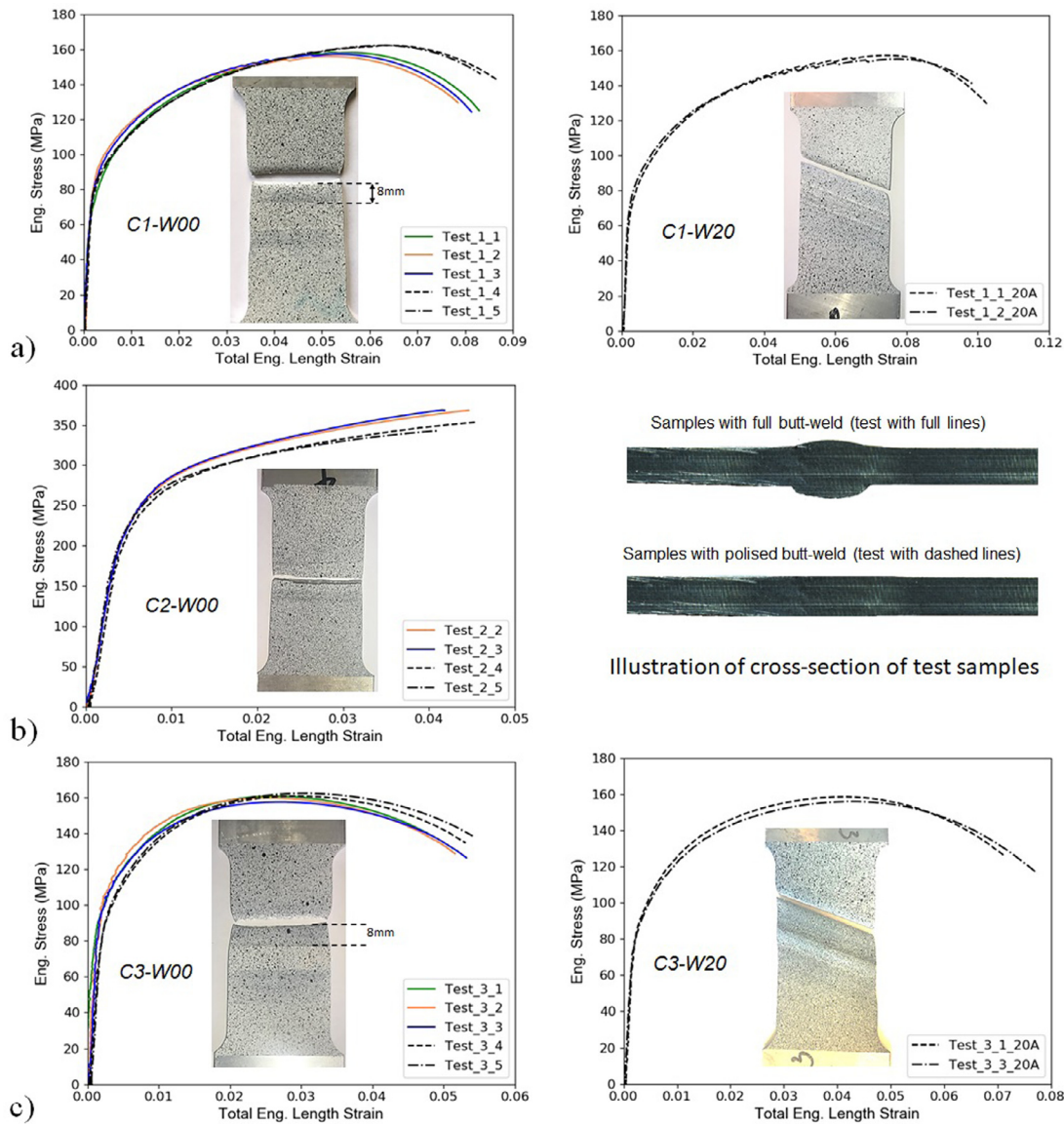
Fig. 11. Cross-weld tests results: (a) Joint C1, (b) Joint C2 and (c) Joint C3. Full lines are shown for test results with full butt-welds, and dashed lines for tests with polished flat ones.

follows [31]:

$$\sigma_{eq} = \frac{\sigma}{\left(1 + \frac{2R}{a}\right)\left[ln\left(1 + \frac{a}{2R}\right)\right]} \tag{6}$$

in which a is the minimum radius and R is the radius of curvature of the neck, see Fig. 14 for illustration. The neck geometry was approximated by the empirical relation proposed by Le Roy et al. [32] as:

$$\frac{a}{R} = 1.1\left(\varepsilon_p - \varepsilon_p^n\right) \tag{7}$$

where ε_p is the equivalent plastic strain and ε_p^n represents its corresponding value at the incipient necking. Fig. 14 shows an illustration of the equivalent stress–plastic strain curves calculated up to fracture using Eqs. (6) and (7) based on the tensile tests result of HAZ of welded 6060 alloy.

The equivalent stress–plastic strain data were used to calibrate the work-hardening behaviour of HAZ and weld materials up to fracture. To verify the calibration, a 2D axisymmetric element based model of smooth sample tensile testing, see Fig. 13b showing a half model due to symmetry, was established in LS-DYNA and numerical simulations were performed with the calibrated parameters. Fig. 10 shows the comparison between the experimental and numerical results of all the tests for HAZ and weld materials in terms of engineering stress versus engineering strain in radial directions. As can be seen, the numerical results with the calibrated material parameters were in a reasonable agreement with experimental curves all the way to fracture, especially for the three weld materials with no anisotropy in plastic flow. For the materials exhibiting anisotropy in plastic flow as for HAZ of the welded 7003 alloy, the simulation results with isotropic material model represented the average of the experimental stress–strain curves in the two radial directions (TTD and TD). Assuming insignificant anisotropy in work-hardening behaviour for HAZ and weld materials, the calibrated work-hardening parameters were further used for simulations of cross-weld tension tests.

As shown in Fig. 5, anisotropy in yield strength was observed for the based materials 6060 and 7003. Considering the microstructure of the HAZ materials (Fig. 7) it is reasonable to assume that HAZ materials exhibit a similar anisotropic behaviour. Assuming that the HAZ has the same flow stress ratio between TD and ED as for the base materials, the yield stress of HAZ materials in TD was estimated. The material parameters were summarized in Table 1. It is to note that the material parameters reported for HAZ materials were based on the average of the experimental stress–strain results obtained in HAZ areas. As for the
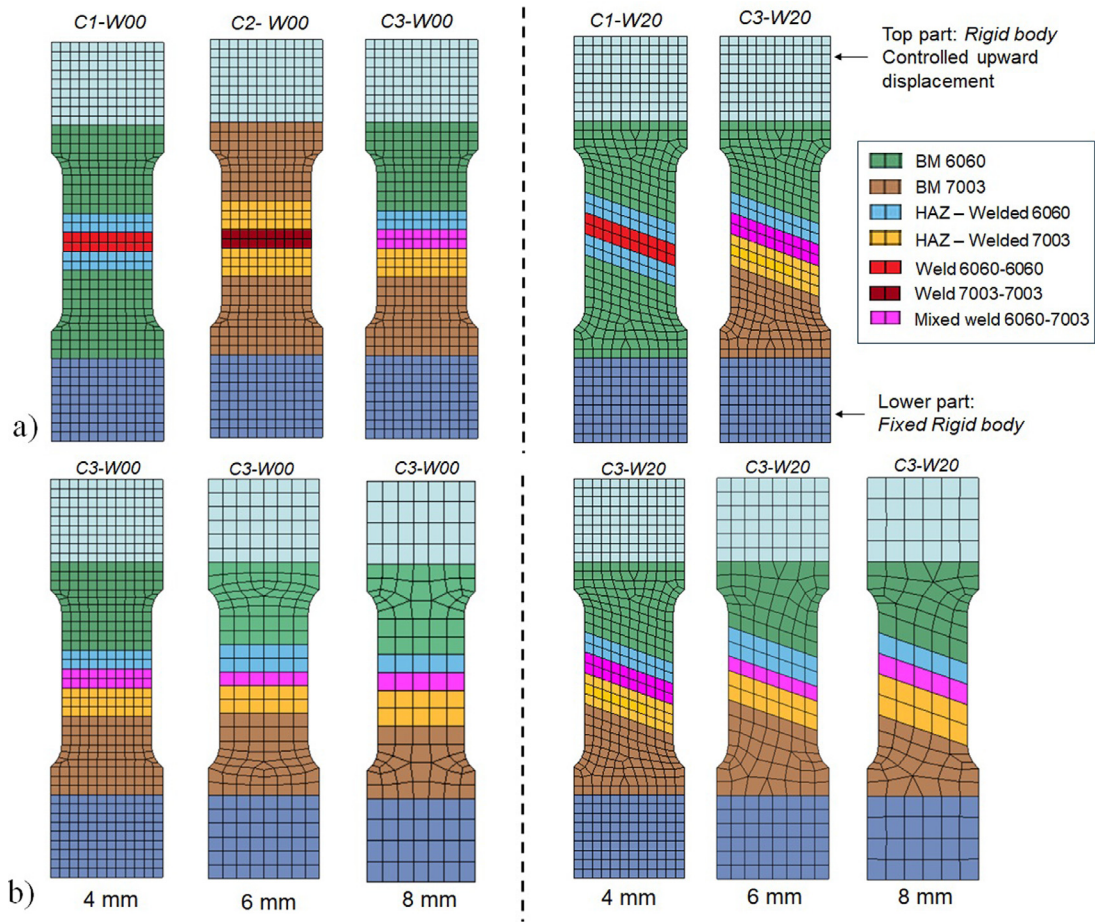
Fig. 12. FEM models of cross-weld tension tests. (a) Reference models with 4 mm mesh size, and (b) Illustration of Joint C3 (6060–7003 joint) test models with different mesh size.
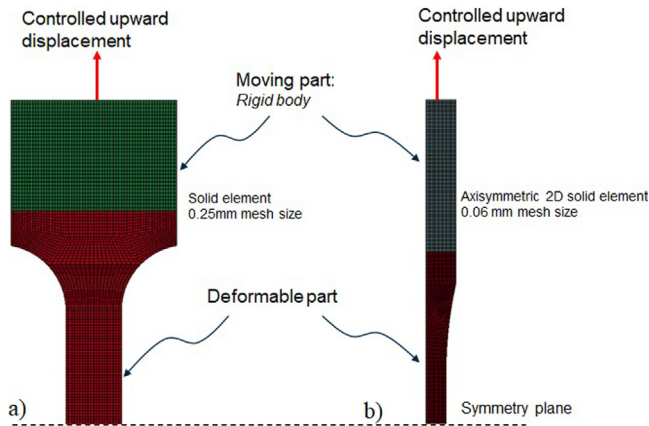

Fig. 13. FEM models of material tests. (a) Flat sample, and (b) Smooth cylindrical sample. Half-models were shown owing to symmetry.
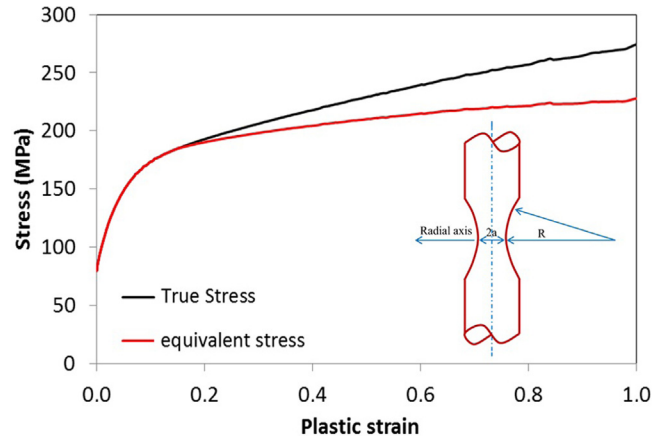

Fig. 14. Illustration of corrected equivalent stress for HAZ of welded 6060.

weld metals, Fig. 10 suggests a negligible plastic anisotropy, and their material properties in TD are assumed to be the same as in ED. All the calibrated material parameters were provided and summarized in Table 1.

3.2. Numerical results and discussions

At first, the conventional modelling approach, namely "mechanical analysis" approach, was investigated, and numerical simulations of

cross-weld tension tests were performed using material parameters of weld metal, HAZ and base materials calibrated from the experimental test results. Since the cross-weld tensile tests were mainly loaded in the transverse direction (TD), the material parameters calibrated in this direction as shown in Table 1 were used. Simulations were carried out using 4 mm mesh models established in the preceding section, with a typical von-Mises yield criterion (i.e. $m = 2$) and a Hershey–Horsford yield function for FCC alloys (i.e. $m = 8$) to verify the effect of the yield functions. The numerical results are compared with experiments
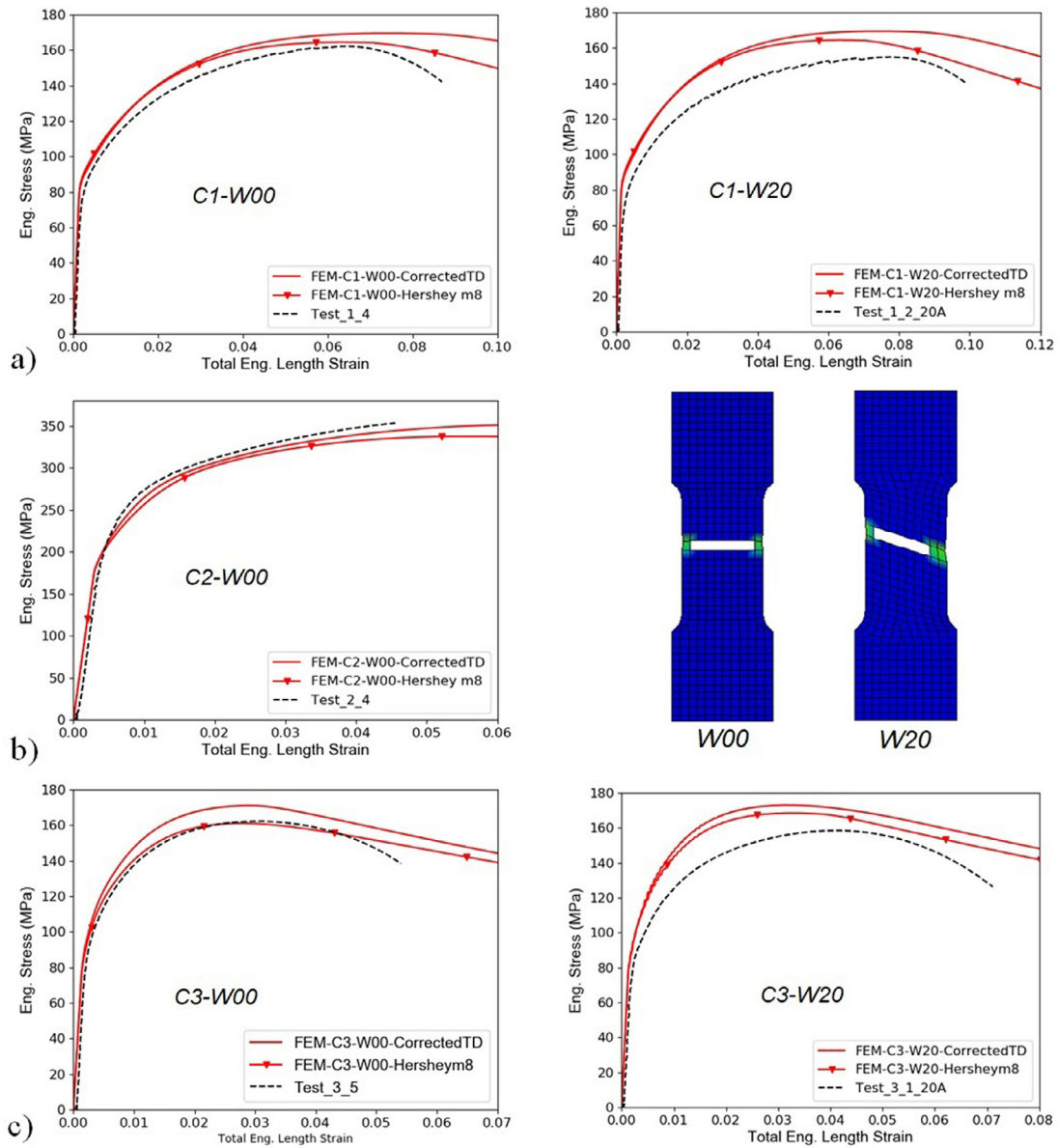
Fig. 15. Numerical results of cross-weld tensile simulations using material parameters calibrated based on testing: (a) Joint C1, b Joint C2 and (c) Joint C3.

in Fig. 15 in terms of engineering stress–engineering strain in the loading direction. To simplify the numerical models, a homogeneous shell thickness was applied in the numerical models. Thus, tests with the polished flat butt-weld were used for comparison and only one experimental curve was shown for the sake of clarity. It can be seen that numerical models with von-Mises yield criterion (i.e. $m = 2$) overestimated the cross-weld tension behaviour in all the tests, except for Joint $C2 - W00$ (i.e. similar material 7003–7003 welded joint). The experimental and numerical results of the latter were very comparable. A higher exponent $m = 8$ of the yield function lowered to some extent the predicted numerical curves in all the simulations, resulting in a better agreement with the experimental results of joints weld angle $\alpha = 0°$. However, numerical models with both $m = 2$ and $m = 8$ overshot the experimental load–displacement behaviour for the joints with the inclined weld, i.e. $\alpha = 20°$. It appears that for the shell element models with a characteristic length of 4 mm, the extensive test programme to provide material inputs to HAZ and weld metal models could not guarantee a perfect prediction of the experimental results. This is probably because the gradient in material properties in the HAZ could not properly be represented by the used 4 mm mesh size.

Previous works of Wang et al. [13] depicted a similar observation. The authors have performed numerical simulations of welded aluminium structures using the properties of the HAZ established based on tensile test data [15]. Material anisotropy of HAZ and base materials were also included in their works, using Barlat and Lian anisotropic yield criterion [33,34]. As complex as the modelling approach may be, the numerical results by Wang et al. [13] were shown to be reasonable, but still overshot the experiments by about 17%. Even though the discrepancy between numerical and experimental results in the present work and Wang et al. [13]'s work may lie within the tolerance range of experimental result variation, the predictive results may not be satisfactory to compensate the cost of the extensive experimental programme and numerical computation for the current approach to be used in an engineering application. It may also be arguable about the validity of the uniform HAZ assumption. The recent numerical method using multi-material elements, in which multiple HAZ properties could be included in a single (large) shell finite element, as proposed by Arif et al. [18] could be a solution to be evaluated in further works.

In the following, a new modelling approach, which is more suitable for engineering application, is proposed. This approach relies on inverse
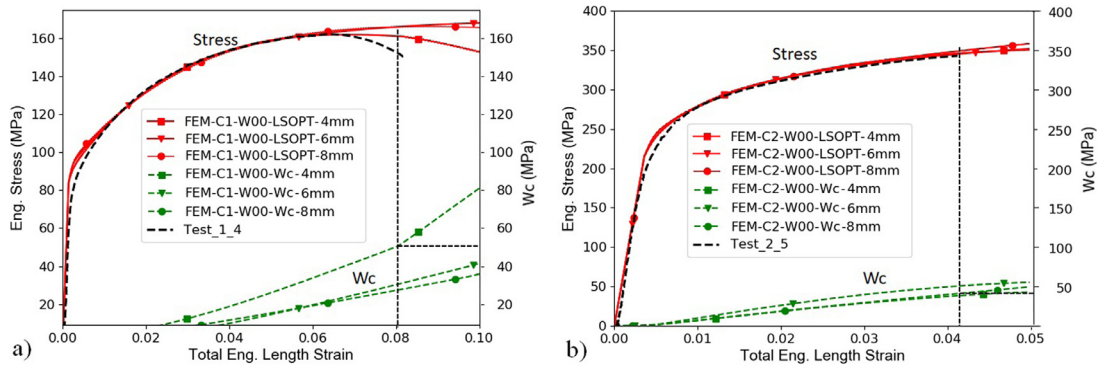
Fig. 16. FEM results with different mesh size of shell elements using LS-OPT: (a) Joint $C1 - W00$ and (b) Joint $C2 - W00$.

modelling of the cross-weld tension behaviour of similar materials joints to obtain the stress–strain behaviour of HAZ and weld materials. In this approach, the following experimental data are required:

- Experimental stress–strain curves of base materials as shown in Fig. 5. These data are used to calibrate the material models for base materials 6060 and 7003 as provided in Table 1.
- Hardness along the cross-weld section as shown in Fig. 6b. Yield stresses of HAZ materials and weld metals were estimated from Vickers hardness (HV) using the following well-established relationship for extruded alloys Al–Mg–Si (Eq. (8)) and Al–Zn–Mg (Eq. (9)) [35–37]:

$$\sigma_0 = 3.0HV - 48.1 \tag{8}$$

$$\sigma_0 = 3.7HV - 100 \tag{9}$$

- Experimental cross-weld tension test data of the joints $C1 - W00$ and $C2 - W00$ of welded similar alloys. The load–displacement curves of these tests were used to optimize the work-hardening behaviour of HAZ and weld metals, using the yields stresses estimated by Eqs. (8) and (9).

Numerical simulations of cross-weld tension tests of the joints $C1 - W00$ and $C2 - W00$ were run using the established model illustrated in Fig. 12a with a von-Mises yield criterion (i.e. $m = 2$). The work-hardening behaviour of the involved HAZ and weld materials was optimized by fitting the global load–displacement behaviour of the simulated joints with the corresponding test results. The optimization was automatically performed using LS-OPT software [38]. Fig. 16 shows the optimization results of the joints $C1 - W00$ and $C2 - W00$. As seen, the global behaviour of cross-weld tension tests was correctly fitted up to the maximum stress, prior to any strain localization. The work-hardening behaviour obtained by LS-OPT optimization is illustrated in Fig. 17 for weld metals of Joints C1 welded 6060–6060 and welded 7003–7003. However, the stress–strain behaviour obtained by LS-OPT optimization may not necessarily be correlated to the realistic properties from the experimental tensile tests shown in Fig. 9. As the main objective of the current approach is to model the welded aluminium structure at the macroscopic level, the local work-hardening properties of HAZ and weld metals obtained by inverse modelling need not to be comparable to the realistic result. Keeping in mind that when the material gradient could not be represented by the industrial mesh size, using the true work-hardening properties of weld metals and HAZ would not be necessary as shown in the first approach. The stress–strain curve of the mixed weld 6060–7003 was then obtained by averaging these data obtained for welded 6060–6060 and welded 7003–7003 joints, see Fig. 17. The obtained model parameters by this approach for the HAZ and weld metals under investigation are shown in Table 1 as an example for the 4 mm mesh models.

To account for fracture, a phenomenological approach to describe ductile fracture presented by Cockcroft and Latham [39] was included
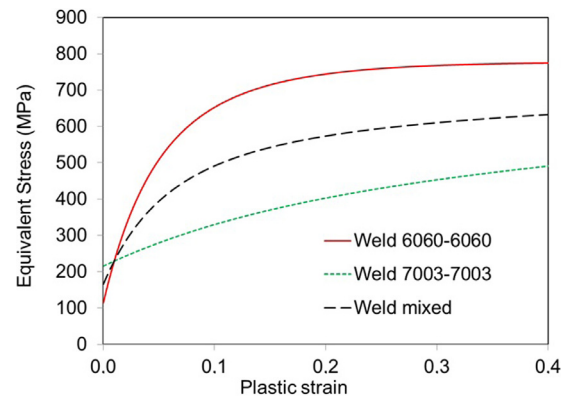

Fig. 17. Weld materials properties obtained by LS-OPT fitting.

in the model. The Cockcroft–Latham (CL) criterion states that fracture occurs when the variable W reaches a critical value W_{cr}, and reads as follows

$$D = \frac{W}{W_{cr}} = \frac{\int_0^{\varepsilon_p} max(0, \sigma_1)d\varepsilon_p}{W_{cr}} \leq 1.0 \tag{10}$$

in which σ_1 and ε_p are respectively the maximum principal stress of the Cauchy stress tensor and the equivalent plastic strain, while D represents the uncoupled ductile damage indicator. The critical value W_{cr} was determined by plotting the evolution of W in the shell-based model together with engineering stress–strain curves as shown in Fig. 16. As seen, W_{cr} was taken out at fracture of the tested specimen.

To verify the proposed approach, numerical simulations of the remaining joints, i.e. $C1-W20$, $C3-W00$ and $C3-W20$, were performed using the plasticity and fracture properties of HAZ and weld materials obtained by the inverse modelling. Fig. 18 shows the simulation results in terms of engineering stress–strain curves of these joints plotted along the experimental ones. As observed, the numerical results were in reasonable agreement with the experiments.

The fracture behaviour was also predicted reasonably. In the simulations of the dissimilar material joints $C3 - W00$ and $C3 - W20$, fracture occurred earlier than in the experiments, see Fig. 18. However, fracture was numerically initiated after reaching the experimental ultimate stress, which is acceptable for general design purposes. In all the verification simulations, fracture was observed in the HAZ of welded 6060 side as in the experiments, see Fig. 19 showing the numerical fracture pattern in cross-weld tension tests of $C1 - W20$, $C3 - W00$ and $C3 - W20$.

The performance of the proposed approach for modelling the welded aluminium structure using larger shell elements, namely 6 mm and 8 mm, was investigated. Fig. 12b illustrates a typical meshing of the cross-weld specimens including the discretization of HAZ and weld
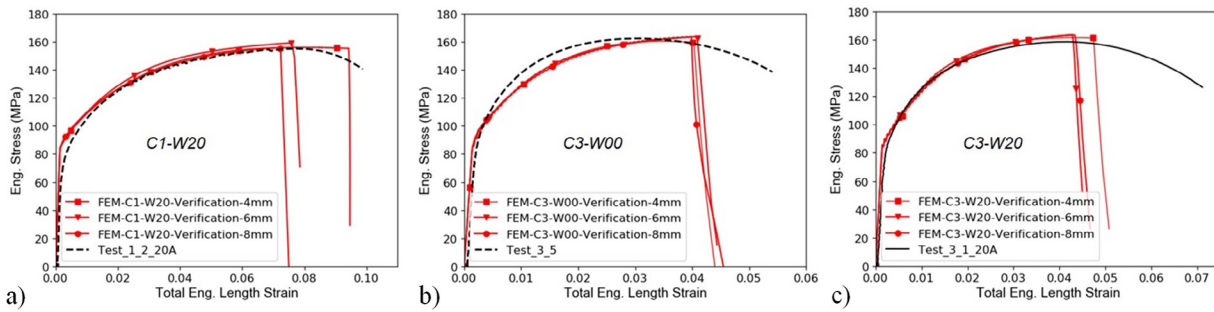
Fig. 18. Comparison between experimental and numerical results using HAZ and weld metal properties calibrated using LS-OPT: (a) Joint $C1 - W20$, (b) Joint $C3 - W00$ and (c) Joint $C3 - W20$.
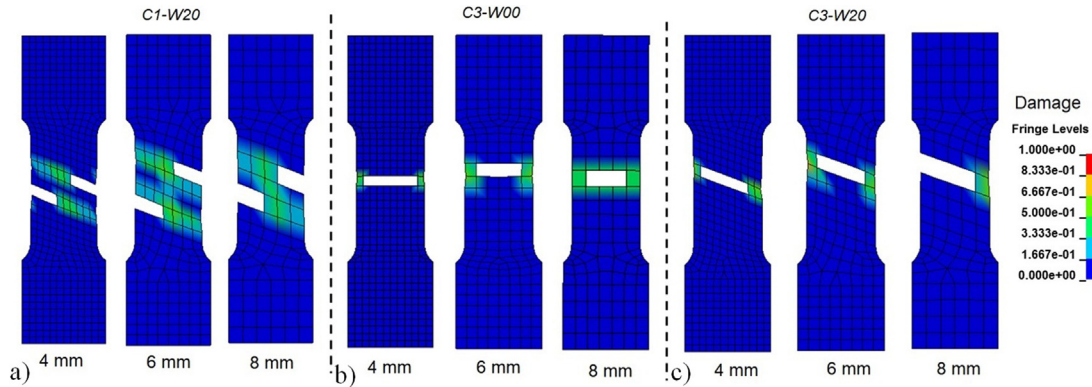

Fig. 19. Predicted fracture in cross-weld tension tests of (a) Joint $C1 - W20$, (b) Joint $C3 - W00$ and (c) Joint $C3 - W20$.

metals parts for the investigated mesh sizes. The same procedure was followed and LS-OPT fitting simulation results were reported in Fig. 16, together with the results using 4 mm shell-based models. Verification simulations were performed and the results were also plotted in Figs. 18 and 19, depicting the predicted stress–strain and fracture behaviours. A good agreement between numerical and experimental results both in terms of load–displacement and fracture behaviour was obtained, suggesting that the novel modelling approach could be a reliable and efficient method for designing butt-welded aluminium structures. However, the validity/applicability of the proposed modelling approach for other kinds of MIG welded joints such as T-joint and corner joints remains open for investigations. Further works could also be done to evaluate the modelling of welded structures in case the HAZ width is much smaller than the currently investigated industrial mesh sizes.

4. Concluding remarks

In the present study, the mechanical and fracture behaviour of welded aluminium thin-walled structures were investigated, experimentally and numerically. Welded connections of both similar and dissimilar materials were first investigated experimentally, using two extruded plates made of 6060 and 7003 in temper T6 as parent materials. The experimental results were used to provide input, calibrate and validate shell element-based models to simulate welded aluminium structures. Two modelling approaches were considered to predict the load–displacement and fracture behaviour of the investigated welded joints. First approach used material model inputs from the experimental testing, assuming uniform HAZ strength. The second modelling approach, which is proposed in this study, relies on inverse modelling of cross-weld tension behaviour of similar materials joints to determine the hardening properties in the HAZ and weld metals. The following concluding remarks could be drawn from this study:

- Experiments have shown that MIG welding process with advanced CMT Pulse technique was suitable for joining similar

and dissimilar aluminium alloys under investigation (6060 and 7003 in temper T6). The quality of the welded connections was satisfactory, reflected by a consistent microstructure, hardness and mechanical properties. The dissimilar material welded joint represented a good mix of the two similar material welded joints.
- Alloy 6060 has a re-crystallized microstructure, while 7003 possesses a fibrous grain structure. The two alloys exhibit to some extent anisotropic properties in strength, work hardening and plastic flow. Anisotropy in plastic flow was also observed in the HAZ of both 6060 welded and 7003 welded joints. On the contrary, all the weld materials demonstrated no such significant anisotropic property.
- The hardness measurement of cross-welded specimens has shown that the soft areas are found in the HAZ for 6060 welded joints and in the weld metal for 7003 welded joints. A corresponding loss in strength of about 40% in comparison with the base materials was observed. The dissimilar material joint represented a good mix of the two similar material joints, showing the soft area located in the HAZ of the 6060 welded side. Tests also revealed that the lowest yield strength of HAZ of the 6060 welded joints are accompanied with the highest ductility in comparison with other materials.
- Cross-weld tension testing of the investigated welded connections depicted a good repetitiveness in test results. The geometry of the butt-weld (i.e. full butt-weld and polished flat butt-weld) showed to have a slight influence on the load–displacement of tested joints, but not on the fracture behaviour. A ductile failure was observed in the HAZ of the 6060 welded sides for the 6060–6060 and 6060–7003 welded joints, while a through-thickness fracture mode was obtained in the weld metal of 7003–7003 welded joint, see Fig. 11. The obtained fracture was consistent with the hardness test results.
- The tensile test results of HAZ, weld metals, and base materials were used to calibrate material model parameters, including the

work-hardening properties of the investigated materials all the way to fracture. The calibration results have confirmed that the Bridgman–Leroy correction formulation (see Eqs. (6) and (7)) could be used as an efficient and reliable method to estimate the work-hardening behaviour after the incipient necking of the isotropic material tested with smooth cylindrical samples.

- Numerical models were established to simulate the cross-weld tension behaviour. In the first modelling approach, the so-called conventional "mechanical analysis", material model inputs were obtained from the experimental testing, assuming uniform HAZ strength. The simulation results showed a reasonable prediction of the experimental load–displacement results. However, the gradient in material properties of HAZ could not be captured with the used large shell elements. It may also be arguable about the validity of the uniform HAZ assumption. The recent numerical method using multi-material elements, in which multiple HAZ properties could be included in a single (large) shell finite element, as proposed by Arif et al. [18] could be a solution to be evaluated in further works.

- The second modelling approach, which was proposed in this study, calls for a numerical inverse modelling to determine the HAZ and weld metal model parameters for structural analyses of welded structures. This proposed approach requires less experimental testing. A good agreement between numerical and experimental results both in terms of load–displacement and fracture behaviour was obtained using shell element-based models with different mesh sizes. The results suggested that the novel modelling approach could be a reliable and efficient method for designing butt-welded aluminium structures. However, the validity/applicability of the proposed modelling approach for other kinds of MIG welded joints such as T-joint and corner joints remains open for investigations. Further works could also be done to evaluate the modelling of welded structures in case the HAZ width is much smaller than the currently investigated industrial mesh sizes.

CRediT authorship contribution statement

Nguyen-Hieu Hoang: Conceptualization, Methodology, Testing, Simulations, Validation, Data curation, Writing – original draft, Writing – review & editing. **David Morin:** Conceptualization, Validation, Writing, Data curation, Project administration. **Magnus Langseth:** Writing – review & editing, Data curation, Funding acquisition.

Declaration of competing interest

The authors declare that they have no known competing financial interests or personal relationships that could have appeared to influence the work reported in this paper.

Acknowledgements

References

[1] F. Mazzolani, En1999 eurocode 9: Design of aluminium structures, in: Proceedings of the Institution of Civil Engineers-Civil Engineering, Vol. 144, (6) Thomas Telford Ltd, 2001, pp. 61–64.

[2] O. Myhr, S. Klokkehaug, H. Fjaer, Ø. Grong, A. Kluken, Modelling of microstructure evolution and residual stresses in processing and welding of 6082 and 7108 aluminium alloys, in: Proc. 5th Int. Conf. on Trends in Welding Research, 1998.

[3] O. Myhr, O. Grong, O. Lademo, T. Tryland, Optimizing crash resistance of welded aluminum structures, Welding J. 88 (2) (2009) 42–45.

[4] O.R. Myhr, O.S. Hopperstad, T. Børvik, A combined precipitation, yield stress, and work hardening model for al-mg-si alloys incorporating the effects of strain rate and temperature, Metall. Mater. Trans. A 49 (8) (2018) 3592–3609.

[5] Z. Zhang, J. Ødegård, O. Myhr, H. Fjær, From microstructure to deformation and fracture behaviour of aluminium welded joints–a holistic modelling approach, Comput. Mater. Sci. 21 (3) (2001) 429–435.

[6] A. Pickett, M. Fouinneteav, S. Gudgeon, V. Robin, J. Christlein, Model characterization and failure analysis of welded aluminium components including process history, Int. J. Crashworth. 12 (5) (2007) 449–463.

[7] Q. Puydt, S. Flouriot, S. Ringeval, F. De Geuser, R. Estevez, G. Parry, A. Deschamps, Relationship between microstructure, strength, and fracture in an Al-Zn-Mg electron beam weld: part II: mechanical characterization and modeling, Metall. Mater. Trans. A 45 (13) (2014) 6141–6152.

[8] N. Nazemi, Identification of the mechanical properties in the heat-affected zone of aluminum welded structures, 2015.

[9] C. Dørum, O.-G. Lademo, O.R. Myhr, T. Berstad, O.S. Hopperstad, Finite element analysis of plastic failure in heat-affected zone of welded aluminium connections, Comput. Struct. 88 (9–10) (2010) 519–528.

[10] A. Alisibramulisi, Through process modelling of welded aluminium structures, 2013.

[11] M. Lozano, M.A. Serrano, C. López-Colina, F.L. Gayarre, J. Suárez, The influence of the heat-affected zone mechanical properties on the behaviour of the welding in transverse plate-to-tube joints, Materials 11 (2) (2018) 266.

[12] M.D. Collette, The impact of fusion welds on the ultimate strength of aluminum structures, in: Proc. ORADS 2007, 2007.

[13] T. Wang, O. Hopperstad, P. Larsen, O.-G. Lademo, Evaluation of a finite element modelling approach for welded aluminium structures, Comput. Struct. 84 (29–30) (2006) 2016–2032.

[14] T. Wang, O. Hopperstad, O.-G. Lademo, P. Larsen, Finite element analysis of welded beam-to-column joints in aluminium alloy EN AW 6082 T6, Finite Elem. Anal. Des. 44 (1–2) (2007) 1–16.

[15] M. Matusiak, P. Larsen, Strength and ductility of welded connections in aluminium alloys, in: Joints in Aluminium-INALCO'98: Seventh International Conference, Woodhead Publishing, 1999, p. 299.

[16] E. Markiewicz, B. Langrand, N. Leconte, J. Fabis, T. Dupuy, A methodology for the viscoplastic behaviour characterisation of spot-weld heat affected materials, J. Mater Process. Technol. 238 (2016) 169–180.

[17] J. Carrier, E. Markiewicz, G. Haugou, D. Lebaillif, N. Leconte, H. Naceur, Influence of the heat affected zone on the dynamic behavior of a welded joint of armoured steel, Int. J. Impact Eng. 104 (2017) 154–163.

[18] W. Arif, H. Naceur, S. Miran, N. Leconte, E. Markiewicz, Fast and accurate multi-material model for the prediction of laser welded structural response, Eng. Comput. (2021).

[19] P. Woelke, B. Hiriyur, K. Nahshon, J. Hutchinson, A practical approach to modeling aluminum weld fracture for structural applications, Eng. Fract. Mech. 175 (2017) 72–85.

[20] M. Fourmeau, T. Børvik, A. Benallal, O.S. Hopperstad, Anisotropic failure modes of high-strength aluminium alloy under various stress states, Int. J. Plast. 48 (2013) 34–53.

[21] S. Zhang, P.G. McCormick, Y. Estrin, The morphology of Portevin–Le Chatelier bands: finite element simulation for Al–Mg–Si, Acta Mater. 49 (6) (2001) 1087–1094.

[22] A. Benallal, T. Berstad, T. Børvik, O. Hopperstad, I. Koutiri, R.N. De Codes, An experimental and numerical investigation of the behaviour of AA5083 aluminium alloy in presence of the Portevin–Le Chatelier effect, Int. J. Plast. 24 (10) (2008) 1916–1945.

[23] J. Kang, R.K. Mishra, D.S. Wilkinson, O.S. Hopperstad, Effect of Mg content on Portevin–Le Chatelier band strain in Al–Mg sheet alloys, Phil. Mag. Lett. 92 (11) (2012) 647–655.

[24] M. Abbadi, P. Hähner, A. Zeghloul, On the characteristics of Portevin–Le Chatelier bands in aluminum alloy 5182 under stress-controlled and strain-controlled tensile testing, Mater. Sci. Eng. A 337 (1–2) (2002) 194–201.

[25] H. Dierke, F. Krawehl, S. Graff, S. Forest, J. Šachl, H. Neuhäuser, Portevin-LeChatelier effect in Al-Mg alloys: Influence of obstacles - experiments and modelling, Comput. Mater. Sci. 39 (1) (2007) 106–112.

[26] J. Robinson, M. Shaw, The influence of specimen geometry on the Portevin-Le Chatelier effect in an Al-Mg alloy, Mater. Sci. A 159 (2) (1992) 159–165.

[27] W. Hosford, A generalized isotropic yield criterion, 1972.

[28] M. Costas, D. Morin, O.S. Hopperstad, T. Børvik, M. Langseth, A through-thickness damage regularisation scheme for shell elements subjected to severe bending and membrane deformations, J. Mech. Phys. Solids 123 (2019) 190–206.

[29] H. Aretz, Applications of a new plane stress yield function to orthotropic steel and aluminium sheet metals, Modelling Simulation Mater. Sci. Eng. 12 (3) (2004) 491.

[30] F. Barlat, H. Aretz, J.W. Yoon, M. Karabin, J. Brem, R. Dick, Linear transfomation-based anisotropic yield functions, Int. J. Plast. 21 (5) (2005) 1009–1039.

[31] P. Bridgman, The stress distribution at the neck of a tension specimen, Trans. ASM 32 (1944) 553–574.

[32] G. Le Roy, J. Embury, G. Edwards, M. Ashby, A model of ductile fracture based on the nucleation and growth of voids, Acta Metall. 29 (8) (1981) 1509–1522.

[33] F. Barlat, K. Lian, Plastic behavior and stretchability of sheet metals. Part I: A yield function for orthotropic sheets under plane stress conditions, Int. J. Plast. 5 (1) (1989) 51–66.

[34] O. Lademo, T. Berstad, O. Hopperstad, K. Pedersen, A numerical tool for formability analysis of aluminium alloys, Part II: Exp. Valid. Steel Grips 2 (2004) 433–437.

[35] O. Grong, Metallurgical modelling of welding, Institute of Materials, 1 Carlton House Terrace, London, SW 1 Y 5 DB, UK, 1997. 605, 1997.

[36] O. Myhr, Ø. Grong, S. Andersen, Modelling of the age hardening behaviour of Al–Mg–Si alloys, Acta Mater. 49 (1) (2001) 65–75.

[37] A. Alisibramulisi, O.R. Myhr, O.-G. Lademo, P.K. Larsen, An experimental investigation of the Heat Affected Zone (HAZ) properties of AA6060 and AA7046 following different heat treatment schedules, in: Proceedings of the 12 Th International Conference on Aluminium Alloys, Yokohama, Japan, 2010.

[38] N. Stander, W. Roux, T. Goel, T. Eggleston, K. Craig, LS-OPT user's manual, Livermore Software Technology Corporation, 2008.

[39] M. Cockcroft, D. Latham, et al., Ductility and the workability of metals, J. Inst. Metals 96 (1) (1968) 33–39.